

DRAFT VERSION APRIL 17, 2018
Typeset using L^AT_EX **modern** style in AASTeX62

ALMA Observations of Molecular Absorption in the Gravitational Lens PMN 0134-0931 at $z=0.7645$

TOMMY WIKLIND,¹ FRANCOISE COMBES,² AND NISSIM KANEKAR³

¹*Catholic University of America*

Department of Physics

620 Michigan Ave NE

Washington, DC 20064, USA

²*Observatoire de Paris, LERMA,*

College de France, CNRS, PSL Univ, Sorbonne University, UPMC

75014 Paris, France

³*National Centre for Radio Astrophysics*

TIFR, Post Bag 3, Ganeshkhind

Pune 411 007, India

(Received January 1, 2018; Revised January 7, 2018; Accepted April 17, 2018)

Submitted to ApJ

ABSTRACT

We report the detection of molecular absorption lines at $z=0.7645$ towards the radio-loud QSO PMN 0134-0931. The CO J=2–1 and HCO⁺ J=2–1 lines are seen in absorption along two different lines of sight to lensed images of the background QSO. The lines of sight are separated by $\sim 0''.7$, corresponding to 5 kpc in the lens plane. PMN 0134-0931 represents one out of only five known molecular absorption line systems at cosmologically significant distances. Moreover, it is also one of three such systems where the absorption occurs in a galaxy acting as a gravitational lens. The absorption lines through the two lines of sight are shifted by $215 \pm 8 \text{ km s}^{-1}$, possibly representing rotational motion in one of the lensing galaxies. The absorption profiles are wide, $\sim 200 \text{ km s}^{-1}$, suggesting that the absorption occurs in a highly inclined disk galaxy with a flat rotation curve and a cloud-cloud velocity dispersion $\sim 30 \text{ km s}^{-1}$. Gravitational lens models require two equal mass galaxies to account for the observed configuration of lensed images. The presence of two galaxies in close proximity means that they might be interacting and potentially merging and the kinematics of the molecular gas may not reflect ordered rotational motion. The column densities of both CO and HCO⁺ are normal for diffuse molecular gas towards one of the lensed images, but significantly higher towards the other. Also, the abundance ratio $N_{\text{CO}}/N_{\text{HCO}^+}$

Corresponding author: Tommy Wiklind
wiklind@cua.edu

is 2 – 3 times higher than in typical diffuse molecular gas. It is plausible that the second line of sight probes denser molecular gas than what is normally the case for absorption.

Keywords: ISM: general, molecules — galaxies: general, high redshift, ISM — (galaxies:) quasars: absorption lines — submillimeter: ISM

1. INTRODUCTION

Molecular absorption lines seen towards flat-spectrum radio-loud QSOs provide an opportunity to study the molecular interstellar medium (ISM) in high redshift galaxies in much greater detail than what is possible with emission lines. Emission studies of molecular gas in high redshift galaxies have mostly been carried out using rotational transitions of CO (e.g. Carilli & Walter 2013). Such studies have provided crucial information on the most massive redshifted systems, ultra-luminous and luminous infrared galaxies, sub-mm galaxies and high- z quasars (e.g. Walter et al. 2003; Daddi et al. 2008; Combes et al. 2013; Tacconi et al. 2013). Emission line strengths decrease with the inverse square of the luminosity distance and it becomes increasingly difficult to detect CO emission in high-redshift galaxies.

Absorption lines have the advantage that they remain observable at practically any distance, with the sensitivity determined only by the strength of the background source. Absorption lines can therefore be used to obtain detailed information about the physical conditions in molecular gas in galaxies at any redshift. In addition, while molecular emission studies are sensitive to dense and warm molecular gas, prevalent in actively star forming galaxies, absorption lines is more likely to arise in the excitationally cold gas, which is prevalent in less active galaxies. Molecular absorption studies towards background continuum sources thus provide a powerful probe of the evolution of normal galaxies and their interstellar medium (e.g. Wiklind & Combes 1995, 1997; Kanekar & Chengalur 2002; Menten et al. 2008; Henkel et al. 2009; Muller et al. 2014).

Once molecular absorption lines have been detected in a galaxy, deeper studies of accessible molecular lines allow detailed characterization of the physical and chemical conditions in the absorbing gas (e.g. Henkel et al. 2005; Bottinelli et al. 2009; Muller et al. 2014). The relative strengths of different absorption transitions of species where the excitation is dominated by the cosmic microwave background (CMB), can be used to determine the CMB temperature (e.g. Wiklind & Combes 1997; Muller et al. 2013). Comparison between the redshifts of different molecular transitions in an absorber can be used to test for cosmological evolution in the fundamental constants of physics (e.g. Wiklind & Combes 1997; Kanekar 2011; Kanekar et al. 2012; 2015b, 2018). Finally, redshifted absorbers provide the opportunity to study molecules whose transitions fall outside atmospheric transparency windows (e.g. molecular oxygen,

water vapor, LiH, etc; Combes & Wiklind 1995; Combes et al. 1995; Combes & Wiklind 1997a,b; Kanekar & Meier 2015a).

The main obstacle to using molecular absorption lines to study molecular gas at high redshift is the scarcity of such systems. Only five molecular absorption line systems at cosmological distances are known. The rarity of these systems is mainly due to the fact that molecular gas is usually found only in the central regions of galaxies, necessitating a small impact parameter with a background continuum source. Hence, molecular absorption is more likely to be found in the host galaxy of an AGN than in an arbitrary intervening galaxy. In addition, a prior knowledge of the redshift is usually necessary to facilitate a search for absorption lines. Of the five known high-redshift molecular absorption line systems, only one was found in a blind search, PKS1830-211 (Wiklind & Combes 1996b). A blind search for redshifted molecular absorption towards 36 radio continuum sources using the Green Bank Telescope (Kanekar et al. 2014) probed redshifts $z \gtrsim 0.85$ but provided only upper limits. A sensitive facility like ALMA can in principle allow a large scale search for molecular absorption line systems at high- z , but unfortunately the presently available observing modes makes such an endeavour unfeasible.

The requirement of a small impact parameter means that when absorption do occur in an intervening galaxy, and the intervening galaxy is sufficiently massive, it acts as a gravitational lens of the background source. Of the five known high redshift molecular absorption line systems, including PMN 0134-0931 discussed in this paper, two have the absorption occurring in the host galaxy of the continuum source: PKS1413+135 at $z \sim 0.247$ (Wiklind & Combes 1994; 1997a) and B1504+377 at $z \sim 0.674$ (Wiklind & Combes 1996a). The remaining three absorption systems occur in galaxies acting as a strong gravitational lens to a background AGN: B0218+357 at $z \sim 0.685$ (Wiklind & Combes 1995), PKS1830-211 at $z \sim 0.886$ (Wiklind & Combes 1996b; 1998; Muller et al. 2014) and PMN 0134-0934 $z \sim 0.765$ (Kanekar et al. 2005). Apart from providing detailed information on the interstellar medium itself, the kinematical information obtained when the absorption occurs in a gravitational lens can also provide information that can be used in modeling the lens itself.

In this paper we describe the detection of CO J=2–1 and HCO⁺ J=2–1 molecular absorption at $z \sim 0.765$ towards the gravitationally lensed QSO PMN 0134-0931. Our Atacama Large Millimeter/submillimeter Array (ALMA) observations and data analysis are described in §2, the peculiar gravitational lens PMN 0134-0931 is described in §3. The results obtained with the ALMA data are presented in §4 and discussed in §5. In this paper we use concordance cosmological parameters from the Planck Collaboration (2016): $H_0 = 69.6 \text{ km s}^{-1} \text{ Mpc}^{-1}$; $\Omega_m = 0.286$; $\Omega_\Lambda = 0.714$.

2. OBSERVATIONS

We observed the CO J=2–1 and HCO⁺ J=2–1 transitions, redshifted into ALMA bands 3 and 4, respectively (hereafter B3 and B4). The observations were done in

three separate visits on September 9 (B4), September 17 and 19 (B3), 2016 under ALMA Cycle 3 project 2015.1.00582.S. The two B3 observations were both done with 40 antennas and PWV¹ ~ 0.5 and 2.0 mm, respectively. The longest baseline was 3.14 km, resulting in a nominal angular resolution² of $0''.35$. The total on-source time was ~ 52 minutes. The B4 observations were done with 38 antennas on a single occasion, with PWV ~ 0.48 mm. The longest baseline was 2.48 km, with a nominal angular resolution of $0''.28$. The total on-source time for the B4 observation was ~ 67 minutes.

The correlator setup for our B3 and B4 observations are shown in Table 1. For each band we used two basebands of width 1.875 GHz and 1920 channels giving a spectral resolution of 976.563 kHz. In the rest frame of the absorber, this corresponds to a velocity resolution of 2.90 km s⁻¹ in B3 and 2.23 km s⁻¹ in B4. In addition, we used two spectral basebands of width 2 GHz with 128 channels in continuum mode. The high resolution basebands were centered on 101.007 and 130.276 GHz, for CO J=2–1 and HCO⁺ J=2–1, respectively. The continuum channels were centered at 91 GHz and 140 GHz, for B3 and B4, each with a combined bandwidth of ~ 4 GHz. The continuum data was used to construct images of the PMN 0134-0931 system. Since these were obtained at different frequency settings than the high spectral resolution basebands, we used continuum levels obtained from the high spectral resolution data in the analysis of the absorption lines.

The data reduction and calibration was done with the CASA³ package following standard procedures. The bright quasar J0006-0623 was used as both bandpass and flux calibrator. The flux calibration was bootstrapped to results from Solar system objects. The overall flux accuracy is better than $\sim 10\%$ in both B3 and B4. Phase calibration was done with J0141-0928 for both B3 and B4.

In addition to the CO J=2–1 and HCO⁺ J=2–1 transitions, the high spectral resolution observations covered the redshifted transitions of HCN J=2–1 ($\nu_0 = 177.263$ GHz), HNC J=2–1 ($\nu_0 = 181.325$ GHz) and H₂O J=3₁₃ – 2₂₀ ($\nu_0 = 183.310$ GHz).

3. THE GRAVITATIONAL LENS PMN 0134-0931

The gravitational lens nature of PMN 0134-0931 was discovered independently by Winn et al. (2002) in a survey of radio continuum sources and by Gregg et al. (2002) in a survey of red QSOs. High resolution radio continuum observations reveal six compact components with a maximum separation of $\sim 0''.7$ (Winn et al. 2003). The lens itself has not been reliably detected as it is overpowered by the glare of the background, $z_s=2.2$ QSO (Gregg et al. 2002; Winn & Keeton 2003). Five of the six radio components (A–E)⁴ have the same spectral index from 1.7 to 43 GHz ($\alpha = -0.69 \pm 0.04$, where $S_\nu \propto \nu^\alpha$), while a sixth component (F) has a much steeper spectral index and is only seen in the $\nu_{obs} \leq 8.4$ GHz radio data. Hence, the F

¹ Precipitable water vapor

² The actual angular resolution depends on the uv-weighting applied in the CLEAN process.

³ Common Astronomy Software Applications: <http://casa.nrao.edu>

⁴ We use the same designation of the lens components as in Winn & Keeton (2003).

component is likely to arise from a second emission component in the background QSO, physically distinct from the flat spectrum component. Differential extinction between the lensed QSO images indicates that the lens contains significant amount of dust (Gregg et al. 2002; Winn & Keeton 2003) with components C, E and D+F being more extinguished than components A and B. Hall et al. (2002) detected Ca II absorption corresponding to $z=0.7645$ in a Sloan Digital Sky Survey spectrum, interpreted as originating in the lens.

The large number of image components of PMN 0134-0931 makes it a unique gravitational lens and it presents a formidable challenge to lens modeling. Keeton & Winn (2003) did a detailed study of this system and concluded that more than one lensing galaxy is needed to account for the five flat-spectrum components. In order to model the steep spectrum component, a second distinct background source is needed. In their best model, a total of eight lens component is expected, of which six are detected: five images of a flat-spectrum radio core (A–E) and three images of a steep spectrum component (F + two unseen images). The two lensing galaxies, called Gal-N and Gal-S in Keeton & Winn (2003), are of similar mass, with $\sigma \sim 120 \text{ km s}^{-1}$. Gal-N is centered $\sim 0''.2$ south of lens component E and Gal-S is centered $\sim 0''.15$ south of component C. The projected separation of the two galaxies is only $0''.4$ (3.2 kpc at the lens redshift $z_l = 0.7645$). The models suggest that the two galaxies are either both oriented in the east-west direction, or the north-south direction, and highly flattened. The presence of high extinction as well as ionized gas, inferred through scatter broadening of the radio images at low frequencies (Winn & Keeton 2003), suggests that the lensing galaxies are gas and dust rich and therefore likely to be spiral galaxies.

Absorption of the HI 21cm line was first detected in the lens of PMN 0134-0931 by Kanekar & Briggs (2003). The 21cm profile shows two broad components, with the strongest HI component matching the Ca II absorption profile of Hall et al. (2002). The total HI column density is $2.6 \pm 0.3 \times 10^{21} \text{ cm}^{-2}$, assuming a spin temperature of 200 K and a covering factor of unity. The total velocity coverage of the HI absorption components is $\sim 500 \text{ km s}^{-1}$. Kanekar et al. (2005) searched for HCO^+ J=2–1 absorption with the IRAM 30m telescope, the 6 cm ground state H_2CO doublet lines with the Green Bank Telescope (GBT) and the 2 cm first rotationally excited state of H_2CO with both the GBT and the Very large Array, as well as 18cm OH absorption towards PMN 0134-0931 using the GBT. While the HCO^+ and H_2CO lines remained undetected, the two main OH lines at 1665 and 1667 MHz, and the two satellite lines at 1612 and 1720 MHz, were detected. The main OH lines have the same overall shape as the HI 21cm absorption. The two satellite lines are in conjugate absorption and emission, indicating a high OH column density, and can be used to probe the evolution of fundamental constants over a look-back time of ~ 6.7 Gyr (Kanekar et al. 2005).

4. RESULTS

4.1. *Millimeter Continuum*

Our ALMA continuum images of PMN 0134-0931 obtained with our ALMA data are shown in Fig. 1. The highest angular resolution ($0''.24 \times 0''.18$) is obtained at 140 GHz using uniform weighting (right panel in Fig. 1). This high resolution continuum image shows the lens components A,B and C as an extended but not resolved component. The D component is clearly separated from the A-C image by $\sim 0''.7$ and the E component is seen close to the A-C complex. We did not detect the F image which has a steep spectrum and is not likely to contribute to the continuum at millimeter wavelengths. The locations and derived parameters of the continuum components are listed in Table 2 and a comparison with the location of radio continuum images from Winn & Keeton (2003) is shown in Fig. 2. The average spectral index is $\alpha = -1.6$ ($S_\nu \propto \nu^\alpha$) which is steeper than at radio wavelengths. This suggests that dust emission from the background source provides a negligible contribution to the rest frame submm continuum. The 140 GHz observations probe the $670\mu\text{m}$ emission from the background QSO and if it had a detectable dust continuum this should make the measured spectral index flatter.

The high angular resolution continuum image is compared with the gravitational lens components in Fig. 2. The location and relative flux levels are taken from Winn & Keeton (2003). We assume that the D component is co-located with the second brightest millimeter continuum region. The other lens components line up very well with the rest of the mm continuum emission. The A, B and C components are not resolved but the mm continuum is extended, consistent with three blended sources, dominated by the A component. The flux ratios should be the same as at low radio frequencies, as long as differential lensing doesn't affect the measured fluxes. Differential lensing could be present if the emission regions of long wavelength radio continuum do not coincide with the millimeter continuum in the background source. The flux ratio between the D and E components is 1.7 ± 0.4 at 140 GHz and 2.2 ± 0.2 at 15 GHz (Winn & Keeton 2003). The error of the mm continuum flux ratio takes a 10% absolute calibration uncertainty into account. If we add the A-C flux contributions at 15 GHz and take the ratio with the D component, we get 7.9 ± 0.3 (Winn & Keeton 2003). The corresponding flux ratio at 140 GHz is 7.7 ± 0.4 . The flux ratio at 91 GHz is slightly lower 6.6 ± 0.5 , but here the A-C and D components are not entirely resolved, making the flux ratio measurement less certain (see Fig. 1). Overall, the flux ratios seen at radio frequencies are consistent with our results at millimeter wavelengths and we detect no significant effect of differential magnification.

4.2. *Molecular Absorption*

We used an aperture with the same size as the restoring beam to extract spectra towards the continuum images A-C and D in PMN 0134-0931. The data cubes used for extracting the spectra were cleaned using Briggs weighting with the robustness set to

0.5. This results in slightly lower angular resolution than that obtained using uniform weighting, but is necessary to maximize the sensitivity while still retaining sufficient angular resolution to separate the continuum components. A uniform weighting produced noisy spectral data and we were not able to definitively assess the absorption properties towards the E component separate from the A-C image.

We detect absorption of CO J=2–1 and HCO⁺ J=2–1 towards both the A-C and D components. The spectra are shown in Fig. 3. The absorption profiles cover a total velocity range of $\sim 400 \text{ km s}^{-1}$ and consist of several distinct components. The depth of the absorption profiles is $\lesssim 10\%$ of the continuum towards components A-C while it is $\sim 40\%$ and 30% towards the weaker D component for CO and HCO⁺, respectively. Overall, the absorption profiles of CO and HCO⁺ are similar, suggesting that they originate in the same molecular gas. Both the CO and HCO⁺ absorption profiles consist of a ‘narrow’ profile (seen to the right in Fig. 3), and a ‘wider’ profile. We fit Gaussian profiles to the absorption lines. The best result is obtained with three Gaussian components for the D component, one for the ‘wide’ and one for the ‘narrow’ profile. The A-C component only requires two Gaussian components to give a good fit. The results from the Gaussian fits are given in Table 3. The combined width of the ‘narrow’ and ‘wide’ CO and HCO⁺ absorption profiles is $\sim 200 \text{ km s}^{-1}$ towards both the A-C and D images. The CO profile towards the D component is even wider, approaching $\sim 250 \text{ km s}^{-1}$. The overall shapes of the profiles are similar towards the A-C and the D continuum components, despite probing molecular gas separated by 5 kpc in the lens plane.

While the overall shapes of the absorption profiles are comparable towards the A-C and the D continuum components, they do shift in velocity by a significant amount. The difference in intensity weighted velocity across the entire absorption profile for the CO and HCO⁺ lines along the two sight lines towards the A-C and D lens images is $212 \pm 6 \text{ km s}^{-1}$. Fitting two Gaussian profiles to each absorption profile gives a velocity difference of $215 \pm 8 \text{ km s}^{-1}$. Combining a Gaussian fit to the ‘narrow’ absorption components and an intensity weighted velocity for the ‘broad’ absorption profiles gives a slightly larger velocity difference of $218 \pm 8 \text{ km s}^{-1}$. All of these estimates are consistent with each other within the errors and we adopt $\Delta v = 215 \pm 8 \text{ km s}^{-1}$ as the velocity difference between the molecular absorption along the A-C and D lines of sight to PMN 0134-0931.

The observed opacity can be directly derived from the normalized flux $F(\nu)$ shown in Fig. 3 as $\tau_{\nu_{obs}} = -\ln(1 - F(\nu))$. If $F(\nu) = 0$ the absorption is saturated and only a lower limit to the column density can be derived. The absorption profiles towards PMN 0134-0931 do not appear to be saturated although the true opacity τ_ν of the absorbing gas may be higher than $\tau_{\nu_{obs}}$ if the filling factor of absorbing gas, f_c , is less than unity:

$$\tau_\nu = -\ln \left[1 - \frac{1}{f_c} (1 - e^{-\tau_{\nu_{obs}}}) \right] \quad (1)$$

Assuming that $f_c = 1$ and consequently, $\tau_\nu = \tau_{\nu_{obs}}$, a lower limit to the column density of both CO and HCO⁺ can be derived from

$$N_{tot} = \frac{8\pi}{c^3} \frac{\nu^3}{g_J A_{J,J+1}} f(T_x) \int \tau_\nu dv, \quad (2)$$

where g_J is the statistical weight of level J , $A_{J,J+1}$ is the Einstein coefficient for transition $J \rightarrow J + 1$, and the function $f(T_x)$ is

$$f(T_x) = \frac{Q(T_x) e^{E_J/kT_x}}{1 - e^{-h\nu/kT_x}} \quad (3)$$

In local thermal equilibrium (LTE), the partition function $Q(T_x) = \sum g_J e^{-E_J/kT_x}$, where E_J is the energy of level J and T_x is the excitation temperature of the molecule in question. The observed quantity needed for deriving the column density is the velocity integrated opacity τ_ν .

The results for CO and HCO⁺ are given in Table 4 for the A-C and D components. It is clear that the opacities of both CO and HCO⁺ are significantly higher towards the D component. This is consistent with the optical reddening reported by Hall et al. (2002). In particular, the CO opacity towards the D component is one of the highest values seen in molecular absorption line systems. This is largely due to the large width of the absorbing profile and not just its depth. The ratio of N_{CO}/N_{HCO+} is ~ 500 towards the A-C component and ~ 1500 towards the D component. Typical column density ratios seen in other absorption line systems range from ~ 670 (B1504+377; Wiklind & Combes 1995) to ~ 800 (PKS1413+135; Wiklind & Combes 1997). In the other absorption systems the CO and/or the HCO⁺ lines are saturated and no estimate of the abundance ratio can be obtained. The high CO-to-HCO⁺ abundance ratio towards the D component suggests that either the molecular gas seen here is of a different nature than the typical diffuse gas observed or that the covering factor $f_c < 1$ for the HCO⁺ absorption.

The J=2–1 transitions of HCN and HNC are included in the high frequency resolution bandpasses in our ALMA observations. None of these lines are, however, detected at a 3σ level. The H₂O J=3₁₃ – 2₂₀ transition is located at the very edge of our B3 data. Although a potential line is seen at 5σ towards the D continuum component, the proximity to the band edge makes this line less reliable. The H₂O line is not detected toward the A-C component.

4.3. Molecular Emission

Since at least one of the lensing galaxies is gas-rich we searched for CO J=2–1 in emission. We extracted a spectrum from the data cube using a circular aperture with a diameter of 1''0 (7.48 kpc at the redshift of the lens) centered halfway between components A-C and D. We binned the spectrum to a velocity resolution of 13.4 km s^{−1}, resulting in a channel to channel noise rms is 95 μJy/beam. No emission

was detected and assuming a velocity width of 200 km s^{-1} the 5σ upper limit to the molecular mass is $3.5 \times 10^9 M_{\odot}$. The molecular mass was estimated using

$$M_{H_2} = \alpha L'_{CO} = 3.25 \times 10^7 \alpha [S_{CO} \Delta v] \nu_{obs}^{-2} D_L^2 (1+z)^{-3} M_{\odot}, \quad (4)$$

where $[S_{CO} \Delta v]$ is expressed in Jy km s^{-1} , the luminosity distance D_L in Mpc and ν_{obs} in GHz. We used $\alpha = 4.6 M_{\odot} (\text{km s}^{-1} \text{ pc}^2)^{-1}$ for the conversion between CO luminosity and H_2 mass.

5. DISCUSSION

5.1. Kinematics

Both the CO J=2–1 and HCO^+ J=2–1 absorption lines toward the A-C lens components extend for $\sim 200 \text{ km s}^{-1}$, divided into two main absorption components. A similar total width is seen for HCO^+ towards the D lens component. The CO J=2–1 absorption towards the D component is even wider, extending over $\sim 250 \text{ km s}^{-1}$. While the absorption seen towards the A-C component may be composed of contributions towards all three continuum images of the background QSO, separated by up to 1.3 kpc in the lens plane, the D component represents a very narrow line of sight through the lens, probably $\lesssim 1 \text{ pc}$. In other molecular absorption line systems the line widths range from a few km s^{-1} to tens of km s^{-1} (e.g. Wiklind & Combes 1997; Wiklind & Combes 1998). Only PKS1830-211 has molecular absorption lines approaching $\sim 100 \text{ km s}^{-1}$ in width (Wiklind & Combes 1996b, 1998; Muller et al. 2014). This system is also gravitationally lensed and provides two lines of sight through the disk of a spiral galaxy. Molecular absorption is seen along both sightlines, with a velocity separation $\sim 148 \text{ km s}^{-1}$, providing a measure of the rotational motion of the lensing galaxy. The absorption profiles seen along the two lines of sight in PKS1830-211 are very different in shape and width and the 100 km s^{-1} line widths are caused by highly saturated absorption lines. The molecular absorption seen towards the QSO B1504+377 at $z=0.67$ also consists of two distinct absorption lines, separated by $\sim 330 \text{ km s}^{-1}$ (Wiklind & Combes 1996a). In this system the absorption occurs in the host galaxy of the QSO and the two absorption lines occur along a single line of sight. The HI 21cm absorption profile extends across the two molecular absorption complexes and shows that this is one continuous absorption system with a total velocity extent approaching 600 km s^{-1} (Kanekar & Chengalur 2008). In this case, both the molecular and atomic absorption is likely to be associated with a fast neutral gas outflow, similar to those seen in lower redshift AGNs (Morganti et al. 2005).

Large line widths, such as the molecular absorption profiles seen towards PMN 0134-0931, can arise if the line of sight passes through an inclined gas-rich disk. The velocity envelope of the absorbing gas obtained by integrating along a line of sight through an axisymmetric disk depends on the inclination of the galaxy, the shape of the rotation curve, the radial extent of the absorbing gas and its velocity dispersion (Kregel & van der Kruit 2004, 2005). A velocity dispersion of $\sim 30 \text{ km s}^{-1}$, a flat

rotation curve and an inclination $i \gtrsim 60^\circ$ produce a velocity profile of width $\sim 200 \text{ km s}^{-1}$. These parameters can be relaxed by making the radial extent of the gas distribution larger. Of course, molecular gas is not smoothly distributed but exists in discrete clouds and clumps. The velocity profile obtained by integrating along a line of sight represents an envelope and the fact that it is largely ‘filled’ with absorbing molecular gas indicates that there are several absorbing clouds along the lines of sight to PMN 0134-0931. Another possibility is that the absorbing profiles are caused by lines of sight penetrating the disk of two galaxies, which happens to have similar relative velocities. The lens models, however, do not favor such a scenario. The presence of two galaxies, with a projected distance of only $\sim 3 \text{ kpc}$ in the lens plane (Keeton & Winn 2003) means that there is a possibility that the lensing galaxies are engaged in a merger process, with disturbed kinematics and non-circular motion, possibly with tidal arms crossing the line of sight to the background QSO.

The velocity difference between the absorption towards the A-C and D lens components is $215 \pm 8 \text{ km s}^{-1}$ (see Sect. 4). This difference is also seen in the HI 21cm and OH 18cm absorption (Kanevar & Briggs 2003; Kanevar et al. 2005; Fig. 4), although in these cases the background continuum sources were not resolved. The two-galaxy configuration implied by the lens model (Keeton & Winn 2003) has one of the galaxies centered just south of lens component C. If this galaxy extends across the A-C and D components, the molecular absorption may probe the rotation of a disk. In this case the absorption can be used to estimate the dynamical mass of one of the lensing galaxies. This, however, requires knowledge of the exact location and orientation of the lensing galaxy. Currently, neither observational data nor the lens models provide such information. A minimum mass can be derived by assuming that the center of the lens is mid-way between the A-C and D components and that the velocity separation probes the rotational velocity of the disk: $M_{\min} \approx 7 \times 10^9 / \sin i \text{ M}_\odot$. However, as discussed above, due to the small projected distance between the two lensing galaxies, they may be gravitationally interacting and, hence, the kinematics of this system may not represent ordered motion.

5.2. Column Density

The high CO column density seen towards the D lens component is unusual among the molecular absorption systems observed to date, both in distant galaxies as well as in our own Galaxy (Lucas & Liszt 1996). The column density ratio $N_{\text{CO}}/N_{\text{HCO}^+}$ is ~ 2 times higher than earlier estimates along Galactic and high- z sightlines, and 3 times higher than what is seen towards the A-C component in PMN 0134-0931. This high abundance ratio does not seem to be due to an anomalously low N_{HCO^+} . The column density of HCO^+ along the D component is $1.7 \times 10^{14} \text{ cm}^{-2}$ (Table 4), significantly higher than what is typically seen in absorption of diffuse molecular gas. Lucas & Liszt (1996) found an average N_{HCO^+} column density of $2.6 \pm 3.4 \times 10^{13} \text{ cm}^{-2}$ in a sample of 17 line of sights through diffuse molecular gas in the Milky Way

galaxy, almost a factor of ten lower than the column density we derive for HCO^+ along the D component. Our estimate is, however, similar to the average HCO^+ column density of $2 \times 10^{14} \text{ cm}^{-2}$ seen in Infrared Dark Clouds (Sanhueza et al. 2012). The CO column density is also significantly higher than any previously value derived from unsaturated absorption lines. This suggests that the absorption towards the D component occurs in a dense molecular cloud core rather than the typical diffuse molecular gas.

This interpretation is corroborated by the HI 21cm absorption profile (Kanekar & Briggs 2005). In Fig. 4 we compare the HI 21cm absorption profile of Kanekar et al. (2012) with that of the HCO^+ J=2–1 absorption profile presented in this paper. The HI profile has the same broad character as seen in the molecular absorption, with similar overall velocity spread. The HI 21cm observations did not resolve the lensing components but comparing the HI profile with the molecular profiles it is possible to distinguish which part of the HI 21cm absorption is associated with the A-C and the D components, respectively (Fig. 4). There are two interesting differences between the mm-wave molecular and atomic absorption profiles; towards the A-C lens component, the CO and HCO^+ absorption consists of two distinct line components while the HI 21cm absorption consists of a single smooth profile. Still, the overall widths are the same. This suggests that the absorbing gas consists of two denser molecular clumps embedded in a smooth atomic component. Towards the D lens component, on the other hand, the CO and HCO^+ absorption profiles consist of three distinct profiles, two of which are much less pronounced in the HI 21cm absorption and in the case of the ‘narrow’ molecular absorption, essentially without any HI absorption altogether. This suggests that this absorption arises in a gas component that is completely molecular. This is consistent with this being a dense molecular cloud, as inferred from the high $N_{\text{CO}}/N_{\text{HCO}^+}$ column density ratio. The OH 1665 MHz absorption towards PMN 0134-0931 closely follows that of HI (Kanekar et al. 2005), with a pronounced absence of OH in two of the HCO^+ and CO absorption components towards the D image. Since line widths of CO and HCO^+ in dark molecular clouds are typically only a few km s^{-1} (Lucas & Liszt 1996; Sanhueza et al. 2012), the overall large line widths seen in PMN 0134-0931 as well as the large N_{CO} and N_{HCO^+} values are simply due to a large number of absorbing molecular clouds lined up along the line of sight.

Kanekar et al. (2012) provide a 4-component Gaussian fit to their OH 1667 MHz spectrum, with two components at positive velocities (relative to $z = 0.7645$) and two at negative velocities. We use this to infer the OH column density towards lens components A-C and D, assuming that, like the mm-wave absorption, the positive velocity OH absorption arises against A-C and the negative velocity absorption against D. The OH column density estimate also requires the covering factors of the A-C and D components. For this, we use the flux densities of the different components measured by Winn & Keeton (2003) and the low-frequency spectral index of $\alpha = -0.69$

(Winn & Keeton 2003) to estimate the fraction of the total flux density at ~ 945 MHz (the redshifted OH 1667 MHz line frequency) in components A-C and component D. We obtain flux density fractions of ≈ 0.85 in components A-C and ≈ 0.15 in component D, assuming that the other components do not contribute significantly to the 945 MHz flux density. For a typical OH line excitation temperature of 10 K, this then yields OH column densities of $N_{\text{OH}} = 2.1 \times 10^{15} \text{ cm}^{-2}$ and $2.1 \times 10^{16} \text{ cm}^{-2}$ against components A-C and D, respectively, assuming that the covering fractions of components A-C and D are the same as their fractional contribution to the total flux density. Comparing these to the HCO^+ column densities along the two sightlines yields HCO^+ to OH column density ratios of ≈ 0.017 and ≈ 0.0082 towards A-C and D, respectively. The former is similar to estimates of this ratio (≈ 0.03) in diffuse gas in both the Milky Way and high- z galaxies (e.g. Lucas & Liszt 1996; Kanekar & Chengalur 2002), but the latter is significantly lower. This reinforces our suspicion that the sightline towards component D is very different from typical sightlines through spiral galaxies.

To summarize, the gravitational lens PMN0134-0931 consists of two galaxies at $z = 0.7645$ with a small projected separation on the sky. The lensing configuration gives rise to six lensed images. Absorption of ionized, atomic and molecular gas probe kinematically distinct lines of sight through this system. The molecular absorption is seen towards two lines of sight, separated by ~ 5 kpc in the lens plane. The absorption lines shift by $215 \pm 8 \text{ km s}^{-1}$ between the two lines of sight, possibly due to the rotational motion of one of the lensing galaxies. The width of the absorption profiles is $\sim 200 \text{ km s}^{-1}$. This suggests that the absorption occurs in an inclined gas-rich disk with an approximately flat rotation curve and a cloud-cloud velocity dispersion of $\sim 30 \text{ km s}^{-1}$. The column densities of CO and HCO^+ towards the A-C component are similar to other extragalactic molecular absorption systems but it is unusually high towards the D component. This is likely due to the presence of molecular gas more dense than the diffuse molecular gas most commonly seen in absorption. The data on the ISM and its kinematics can potentially be used to further refine the lens modeling and help to understand the nature of this intriguing gravitational lens system. The interpretation is currently hampered by the lack of accurate information on the location and orientation of the lensing galaxies.

This paper makes use of the following ALMA data: ADS/JAO.ALMA#2015.1.00582.S. ALMA is a partnership of ESO (representing its member states), NSF (USA) and NINS (Japan), together with NRC (Canada), MOST and ASIAA (Taiwan), and KASI (Republic of Korea), in cooperation with the Republic of Chile. The Joint ALMA Observatory is operated by ESO, AUI/NRAO and NAOJ. The National Radio Astronomy Observatory is a facility of the National Science Foundation operated under cooperative agreement by Associ-

Table 1. ALMA Correlator Setup

ALMA	ν_{cent}	BW	nchan	$\Delta\nu$	Δv
band	GHz	GHz		MHz	km s ⁻¹
B3	89.151	2.0	128	15.24	51.23
	91.023	2.0	128	15.24	50.18
	101.068	1.875	1920	0.98	2.90
	103.007	1.875	1920	0.98	2.84
B4	128.318	1.875	1920	0.98	2.28
	130.276	1.875	1920	0.98	2.25
	140.318	2.0	128	15.24	32.54
	142.206	2.0	128	15.24	32.12

NOTE— ν_{cent} denotes the central frequency of a each spectral window.**Table 2.** PMN 0134-0931 Continuum components

Component	ν_{obs}	RA	DEC	Integrated flux	Peak flux	Deconvolved size	PA
	GHz	J2000.0		mJy	mJy/beam	mas	deg
(1)	(2)	(3)	(4)	(5)	(6)	(7)	(8)
A–C	90.09	01:34:35.668	-09:31:02.909	52.20±2.7	44.2±1.4	219±56×191±102	176±8
	141.3	01:34:35.667	-09:31:02.886	27.54±0.87	20.74±0.41	146±14×80±27	42±12
D	90.09	01:34:35.701	-09:31:03.263	7.92±0.17	6.97±0.08	240±25×121±36	157±11
	141.26	01:34:35.701	-09:31:03.275	3.57±0.14	3.62±0.08	—	—
E	90.09	—	—	—	—	—	—
	141.26	01:34:35.684	-09:31:02.680	2.10±0.26	1.36±0.11	174±50×128±116	45±75

NOTE—Component D: 141.26 GHz is an unresolved point source; Component E: 90.09 GHz, angular resolution not sufficient to resolve component.

ated Universities, Inc. NK acknowledges support from the Department of Science and Technology via a Swarnajayanti Fellowship (DST/SJF/PSA-01/2012-13).

REFERENCES

- Bottinelli, S., Hughes, A.M., van Dishoeck, E.F., et al. 2009, *ApJL*, 690, 130
- Carilli, C.L. & Walter, F. 2013, *ARA&A*, 51, 105
- Combes, F. & Wiklind, T. 1995, *A&A*, 303, L61
- Combes, F. & Wiklind, T. 1997a, *A&A*, 486, L79
- Combes, F. & Wiklind, T. 1997b, *A&A*, 334, L81
- Combes, F., Garca-Burillo, S., Braine, J., et al. 2011, *A&A*, 528, 124
- Combes, F., Garca-Burillo, S., Braine, J., et al. 2013, *A&A*, 550, 41
- Daddi, E., Dannerbauer, H., Elbaz, D., et al., 2008, *ApJL*, 673, 21

Table 3. Gaussian fit parameters

Component	HCO ⁺ (2-1)			CO(2-1)		
	Peak	v	Δv	Peak	v	Δv
	mJy/beam	km s ⁻¹	km s ⁻¹	mJy/beam	km s ⁻¹	km s ⁻¹
A-C	0.076 ± 0.015	73.80 ± 6.41	39.70 ± 9.14	0.228 ± 0.009	70.38 ± 0.96	30.17 ± 1.35
	0.064 ± 0.024	169.69 ± 4.74	15.05 ± 6.72	0.159 ± 0.013	171.83 ± 0.91	13.15 ± 1.28
D	0.216 ± 0.016	-166.65 ± 3.12	36.21 ± 4.76	0.299 ± 0.047	-161.21 ± 14.99	53.10 ± 16.45
	0.330 ± 0.020	-115.65 ± 1.59	15.05 ± 2.26	0.356 ± 0.136	-117.96 ± 2.88	15.25 ± 6.51
	0.232 ± 0.030	-46.22 ± 1.10	22.85 ± 1.64	0.468 ± 0.064	-48.46 ± 2.85	22.75 ± 4.10

NOTE—The error estimates of the Gaussian components are derived from the covariance matrix of the non-linear fit.

Table 4. Opacity and column densities

Transition	Component	Δv	σ_τ	$\int \tau_\nu dv$	N
		km s ⁻¹		km s ⁻¹	cm ⁻²
CO(J=2-1)	A-C	4.48	0.017	5.25 ± 1.20	$1.80 \pm 0.41 \times 10^{16}$
	D	4.48	0.013	70.26 ± 6.96	$2.40 \pm 0.24 \times 10^{17}$
HCO ⁺ (J=2-1)	A-C	5.79	0.036	7.20 ± 0.65	$3.55 \pm 0.32 \times 10^{13}$
	D	5.79	0.070	35.14 ± 3.21	$1.73 \pm 0.16 \times 10^{14}$

NOTE— σ_τ refers to the 1σ noise in the opacity measured from the normalized flux.

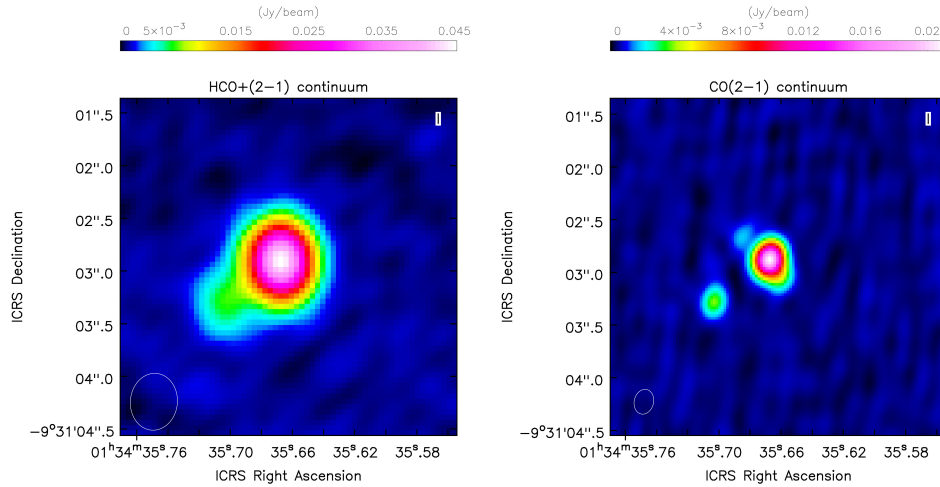


Figure 1. Continuum emission from the background QSO PMN 0134-0701. **Left:** 90 GHz continuum, **Right:** 141 GHz continuum. The highest angular resolution is achieved with the 141 GHz image, done with uniform weighting. In this case the restoring beam is $0''.24 \times 0''.18$ with a position angle of -13.7° . The 90 GHz image has a restoring beam of $0''.54 \times 0''.45$ with a position angle of -5.4° .

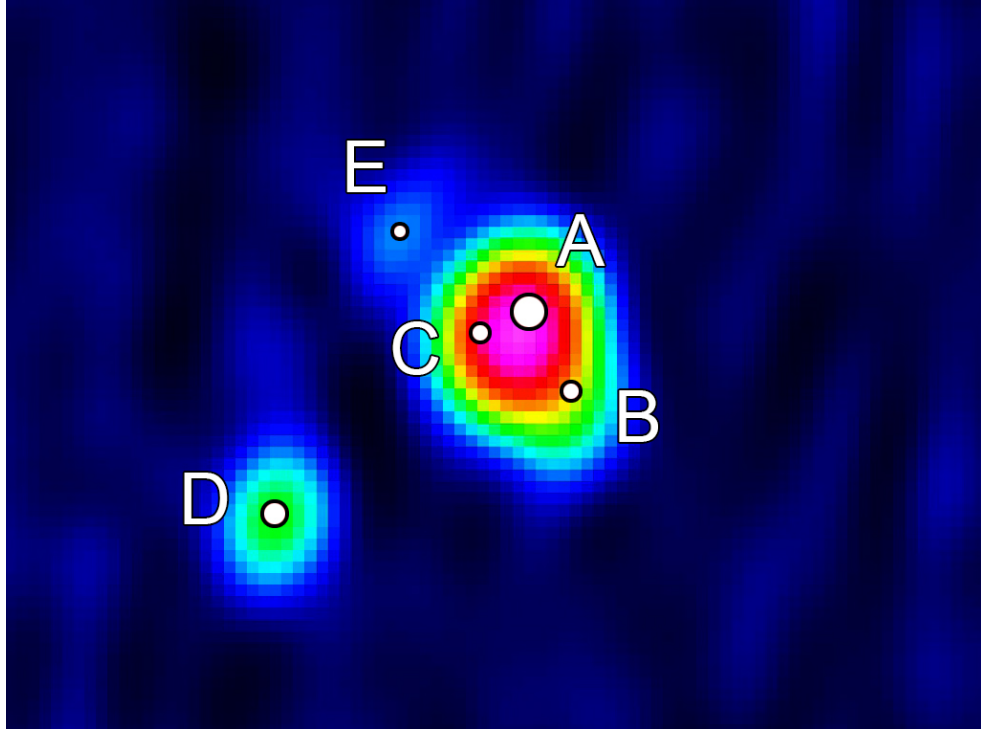


Figure 2. The 141 GHz continuum image of PMN 0134-0931 with uniform weighting. The lens components A–E from Winn & Keeton (2003) are shown. The overlay was done by fixing the D component to the unresolved millimeter continuum below the main continuum component. The relative offsets of the lens components from Winn & Keeton (2003) were then used for the A–C and E components. The F component is not shown as it is a steep spectrum radio source and unlikely to contribute any continuum at 141 GHz. The size of the lens components corresponds to the approximate continuum strength at long radio wavelength and may not reflect the true relative strength at mm wavelengths. The separation between A and D is $0''.68$, corresponding to 5 kpc in the lens plane.

- | | |
|---|---|
| Hall, P.B., Richards, G.T., York, D.G., et al. 2002, <i>ApJL</i> , 575, 51 | Kanekar, N., Gupta, A., Carilli, C.L., Stocke, J.T., Willett, K.W. 2014, <i>ApJ</i> , 782, 56 |
| Henkel, C., Jethava, N., Kraus, A., et al. 2005, <i>A&A</i> , 440, 893 | Kanekar, N. & Meier, D.S. 2015a, <i>ApJL</i> , 811, 23 |
| Henkel, C., Menten, K.M., Murphy, M.T., et al. 2009, <i>A&A</i> , 500, 725 | Kanekar, N., Ubachs, W., Menten, K.M., et al. 2015b, <i>MNRAS</i> , 448, L104 |
| Kanekar, N. & Chengalur, J.N. 2002, <i>A&A</i> , 381, L73 | Kanekar, N., Gosh, T., Chengalur, J.N. 2018, <i>PhRvL</i> , 120, 1302 |
| Kanekar, N. & Briggs, F.H. 2003, <i>A&A</i> , 412, L29 | Keeton, C.R. & Winn, J.N. 2003, <i>ApJ</i> , 590, 39 |
| Kanekar, N., Carilli, C.L., Langston, G.I., et al. 2005, <i>PhRvL</i> , 95, 1301 | Kregel, M & van der Kruit, P.C. 2004, <i>MNRAS</i> , 352, 787 |
| Kanekar, N. & Chengalur, J.N. 2008, <i>MNRAS</i> , 384, L6 | Kregel, M & van der Kruit, P.C. 2005, <i>MNRAS</i> , 358, 481 |
| Kanekar, N. 2011, <i>ApJL</i> , 728, 12 | Lucas, R. & Liszt, H. 1996, <i>A&A</i> , 307, 237 |
| Kanekar, N., Langston, G.I., Stocke, J.T., Carilli, C.L., Menten K.M. 2012, <i>ApJL</i> , 746, 16 | Menten, K.M., Güsten, R., Leurini, S., et al. 2008, <i>A&A</i> , 492, 725 |
| | Morganti, R., Tadhunter, C.N., Oosterloo, T. 2005, <i>A&A</i> , 444, L9 |

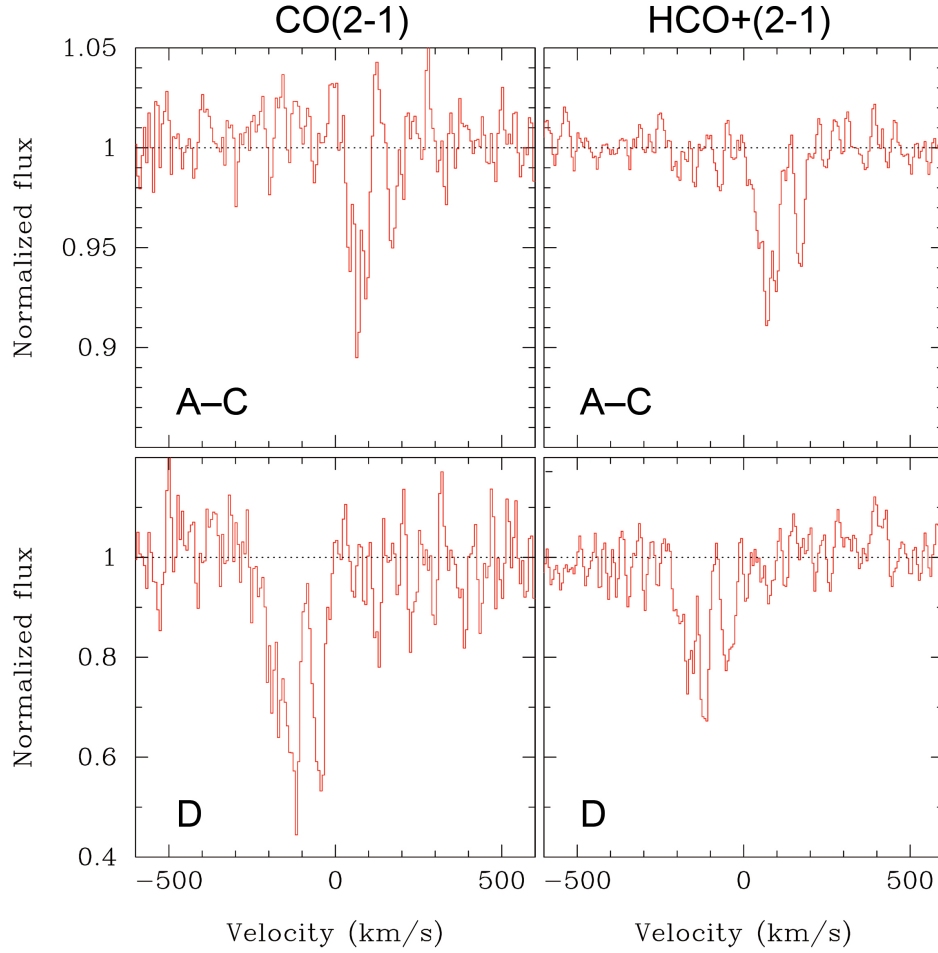


Figure 3. The J=2–1 absorption spectra of CO and HCO^+ towards the A-C lens component (top panels) and the D lens component (bottom panels). The velocity scale is relative to a redshift $z = 0.7645$ and the continuum levels have been normalized to unity.

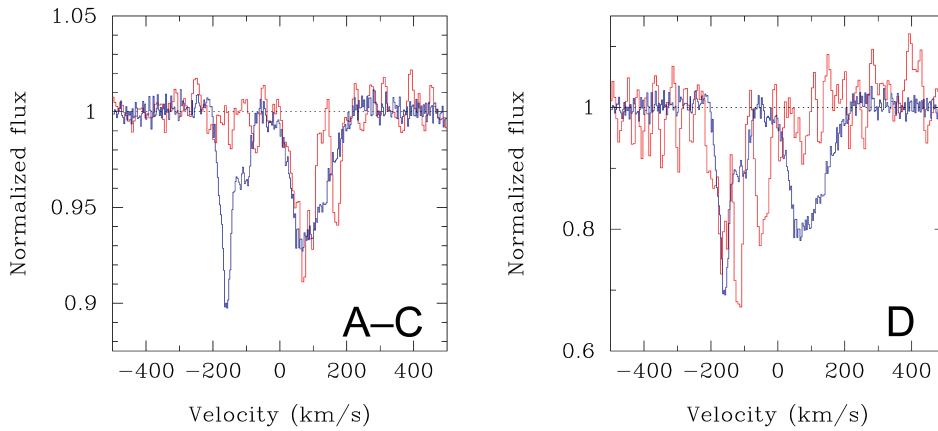


Figure 4. Comparison of the HI 21cm absorption (blue line) from Kanekar & Briggs (2003) with the $\text{HCO}^+(2-1)$ absorption observed with ALMA (red line) seen through the two continuum components A-C and D.

- Muller, S., Muller, H.S.P., Black, J.H., et al. 2016, A&A, 595, 128
- Muller, S., Muller, H.S.P., Black, J.H., et al. 2017, A&A, 606, 109
- Planck Collaboration, et al. 2016, A&A, 594, 13
- Sanhueza, P., Jackson, M., Foster, J.B., et al. 2012, ApJ, 756, 60
- Tacconi, L.J., Neri, R., Genzel, R., et al. 2013, ApJ, 768, 74
- Walter, F., Bertoldi, F., Carilli, C., et al., 2003, Nature, 424, 406
- Wiklind, T. & Combes, F. 1994, A&A, 286, L9
- Wiklind, T. & Combes, F. 1995, A&A, 299, 382
- Wiklind, T. & Combes, F. 1996a, A&A, 315, 86
- Wiklind, T. & Combes, F. 1996b, Nature, 379, 139
- Wiklind, T. & Combes, F. 1997a, A&A, 328, 48
- Wiklind, T. & Combes, F. 1997b, ApJ, 500, 129
- Winn, J.N., Lovell, J.E.J., Chen, H.-W., et al. 2002, ApJ, 564, 143
- Winn, J.N., Kochanek, C.S., Keeton, C.R., Lovell, J.E.J. 2003, ApJ, 590, 26